Journal of Materials Chemistry C

ROYAL SOCIETY OF CHEMISTRY

PAPER

View Article Online
View Journal | View Issue



Cite this: J. Mater. Chem. C, 2026, 14, 5720

# Hybrid copper–silver nanoparticle inks and their performance under thermal and photonic sintering

David Pervan,[ab] Robyn Worsley,[ab] Anil Bastola,[a] Christopher Tuck,[a] Ricky Wildman,[a] Richard Hague[a] and Edward Lester *[b]

Silver (Ag) remains the dominant conductor for two-dimensional (2D) printed electronics applications. Whilst copper (Cu) is significantly cheaper and has comparable conductivity, it has found limited use to date due to its tendency to rapidly oxidise, which is detrimental to the electrical performance of printed features. Whilst oxidation may be avoided through ultra-fast photonic sintering, the need here for new and high capital expenditure slows down any transition from silver to copper. In this work, we investigate the addition of small amounts of Ag to Cu nanoparticle (NP) inks *via* a one-step continuous hydro/solvothermal process, with the aim of mitigating the effects of Cu oxidation under thermal sintering for the additive manufacture of functional Cu components. An *in situ* scanning electron microscopy (SEM) technique was used to visualise thermal sintering and the associated mass transport phenomena for Cu and Ag nanoparticles separately, in order to better understand the sintering behaviour of Cu–Ag composite films. The electrical performance of these thermally sintered hybrid films was compared with that of photonically sintered samples. In the case of intense pulsed light and laser-based techniques, sheet resistance values of ~0.1 and ~0.2 Ω sq$^{-1}$ were obtained respectively for Cu-only samples; the Cu NPs did not oxidise and thus Ag addition was superfluous. However, following thermal sintering in air, Cu-only NP samples were found to be oxidised and non-conductive. Cu NPs with 25 wt% Ag, sintered under the same conditions, demonstrated sheet resistance values of ~1 Ω sq$^{-1}$. This improvement was attributed to Ag mobilisation and the subsequent formation of a continuous network of conductive pathways. Sheet resistance improvements were observed with as little as 3 wt%. Ag addition. This phenomenon was further investigated through theoretical simulations, in order to inform ink formulation and post-processing recommendations, to obtain the highest conductivity for the smallest Ag addition.

Received 4th November 2025,
Accepted 6th February 2026

DOI: 10.1039/d5tc03927d

rsc.li/materials-c



## Introduction

Conventional electronics are typically manufactured using techniques such as photolithography,[1] vacuum deposition,[2] and electroless plating.[3] Each of these approaches involves multiple stages, expensive equipment and the production of hazardous chemical waste.[4] Importantly, in many cases, manufacture is subtractive, meaning that much of the deposited functional material is removed, for example through etching processes, in order to produce the desired circuitry design. This material cannot be recovered, leading to increased wastage of valuable resources. In contrast, additive manufacturing techniques use digital control to selectively deposit the active materials in only the areas required, building electronic devices in a bottom-up manner. Two-dimensional (2D) printing techniques in particular enable the manufacture of thin, lightweight, and cost-efficient electronic systems on a wide variety of substrates, with extremely low levels of materials wastage. This is of particular importance when working with precious conductive metals. Printed electronics research has surged in recent years, with a diverse range of devices, including organic photovoltaics,[5] flexible batteries,[6,7] electro-optic devices,[8–10] field effect transistors, thin film transistors,[11–15] sensors[16–20] and radio frequency identification tags[21,22] being demonstrated, using a variety of deposition techniques, substrates and materials.

Nanoparticle (NP) suspensions have received extensive attention in the field of printed electronics, in part due to the ease with which they may be formulated into well dispersed, stable, and printable inks. Furthermore, as a result of their large surface area, and subsequently high surface energy, the sintering or melting of nanoparticles during post-processing

[a] Centre for Additive Manufacturing (CfAM), Faculty of Engineering, University of Nottingham, Nottingham, NG7 2RD, UK
[b] Advanced Materials Research Group, Faculty of Engineering, University of Nottingham, Nottingham, NG7 2RD, UK. E-mail: Edward.Lester@nottingham.ac.uk

requires a relatively low energy input compared to the respective bulk materials.[23] Metallic NPs are therefore an attractive candidate for the deposition of conductive tracks for printed electronic applications.

To date, the majority of literature regarding the printing of metal NP inks is focused on silver, and less so on copper. This preference for silver, despite its higher relative cost, is largely due to practical advantages, *e.g.*, lower sintering temperatures and low levels of oxidation and agglomeration.[4,24–30]

Notwithstanding these advantages, copper nanoparticles (Cu NPs) possess a similar conductivity to silver when sintered, and are significantly cheaper. However, Cu NPs have an inherent tendency to oxidise in ambient conditions, posing a major obstacle to their use as a conductive material in printed electronics. Oxidation renders the NPs electrically insulating and this undesirable oxide formation reaction greatly accelerates at the elevated temperatures required for sintering.[31] Coating Cu NPs with a protective layer or 'shell' is one well-documented approach to overcome this challenge.[32] These shells are intended to create a physical barrier to oxidation by preventing contact between the Cu NP surface and the surrounding air during the sintering process. They may consist of a polymer,[33–35] various organic ligands,[36] amorphous carbon,[37] graphene-based materials,[38] and even inorganic components such as silica[39] or an inert metal.[40] However, any shell material possessing a lower conductivity, or an insulating nature, suppresses the electrical performance of the subsequent printed pattern. Silver shells, amongst other materials, are a widely reported route to preventing Cu oxidation, since they do not appear to reduce the overall conductivity.[41]

Reports suggest that an Ag shell is able to protect a Cu NP core from oxidation at temperatures between 100 °C and 400 °C,[42–45] with the great majority of studies stating a temperature limit between 150 and 250 °C.[46–59] Above this temperature limit, the Ag shell starts to 'de-wet' the core, thereby leaving the Cu surface exposed to oxidation. Ag delamination is reported to be dependent on the thickness of the Ag shell, which in turn depends on the synthesis methodology, but is independent of the sintering atmosphere *i.e.* whether sintered in air[52] or under inert[60] conditions. Some reports suggest that upon de-wetting, the Ag NPs migrate into necks formed between adjacent Cu particles,[47,52,53,60–64] however, no theoretical or experimental investigations have been conducted to study the impact of such Ag accumulation on the electrical resistance of printed samples. In any case, the increased material and processing costs associated with the Ag content and methodology required for shell formation (multiple sequential batch processes are typically employed) detract from the initial benefits of selecting a Cu conductor, whilst de-wetting of the Ag shell above certain temperatures negates the process and could well limit the post-deposition sintering capability of the Cu–Ag core–shell material.

Thermal sintering of Cu NPs commonly requires temperatures in excess of 200 °C with long exposure times. Another approach towards avoiding oxidation is to perform this process in an inert atmosphere *via* a sealed chamber.[65,66] Indeed, this method is also adopted in cases where inks are simple mixtures of discrete Cu and Ag particles.[67,68] Such blended inks are employed to reduce the costs, decrease the sintering temperatures, and increase conductivity as compared to Cu-only systems, without the necessity for the complex synthesis procedures associated with core–shell dispersions. However, without the oxidation protection of an Ag shell, inert sintering atmospheres are often necessary; such processing requirements tend to limit the applicability of thermal sintering approaches to research based experiments only, as the need for low-oxygen environments cannot always be met, or is incompatible with high-throughput, large scale industrial processes such as roll-to-roll manufacturing.

Conversely, photonic techniques are capable of sintering metallic nanoparticles within milliseconds (before any oxidation can occur) through the rapid heating of a spatially confined volume of deposited material. Photonic sintering techniques have been increasing in popularity over recent years through the development of Intense Pulsed Light (IPL)[69–71] and laser irradiation[72–75] approaches. Both methods have demonstrated the successful sintering of copper, without oxidation, resulting in resistivities approximately 3× higher than that of the bulk material.[69,75] However, to date, thermal sintering remains the most commonly used post-processing approach, with much of the work on photonic techniques limited to academic research.[76,77]

In this study, we show how the addition of small amounts ($\leq$25 wt%) of Ag NPs to Cu NPs can produce excellent levels of conductivity, even when films are sintered at lower temperatures and in an ambient air, oxygen-containing environment. Hybrid Cu–Ag NP dispersions were synthesised using a one-step continuous hydro/solvothermal method. Such synthesis techniques are capable of generating a wide variety of functional nanomaterials, at scale, and with a high degree of control over product characteristics. Variations in process parameters such as reactor temperature and pressure, precursor type and concentration, and flow rates or flow ratios, can influence the final particle size, shape, crystallinity, and surface chemistry.[78–81] The hybrid dispersions in this work are a simple mixture of Ag and Cu NPs, rather than Cu–Ag core–shell particles or alloyed materials, both of which typically require more complex or multi-stage syntheses; the single-step continuous flow method utilised in this work enables the high throughput ink production necessary for large-scale additive manufacture. Furthermore, these Cu–Ag inks may be sintered without the necessity for sophisticated, inert-atmosphere instrumentation. Hybrid Cu–Ag samples were deposited onto glass substrates *via* bar coating and post-processed using a traditional hot plate-based thermal sintering procedure in ambient air. To the best of our knowledge, this is the only report of a Cu–Ag hybrid ink which can be produced scalably, using a single-step, continuous-flow method, that can also be post-processed using only basic equipment, thus showing true promise for the large-scale and facile production of conductive electronic features. The electrical performance and oxidation stability of such thermally-treated films were investigated and compared with samples processed using IPL and laser sintering techniques. NP behaviour during thermal sintering was extensively studied *via in situ* scanning electron microscopy (SEM) techniques, and these observations were used to inform theoretical simulations intended to aid the optimisation of future

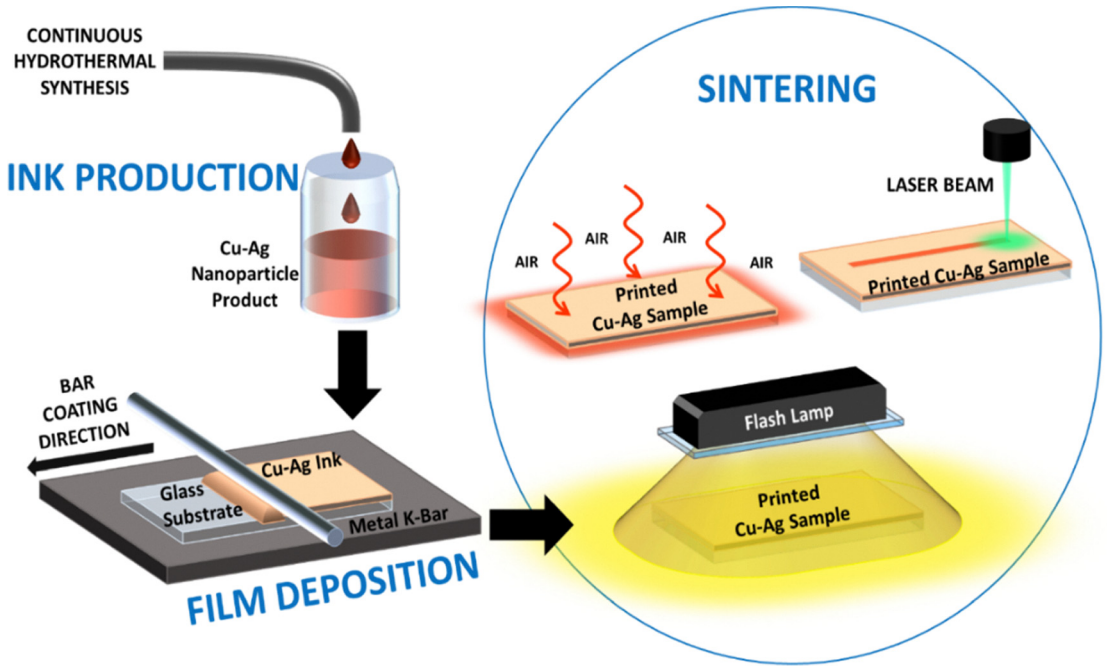


Fig. 1 Schematic showing the overall workflow, from ink production and film deposition through to the various post-processing sintering approaches.

ink formulations and post-processing approaches. The overall scheme of work is shown in Fig. 1.

## Experimental

### Materials and methods

**Metallic nanoparticle synthesis and ink formulation.** In brief, a one-step continuous supercritical hydrothermal method, which has been explored and described extensively in previous reports[79,80,82] was utilised to synthesise the nanoparticles *via* copper nitrate ($Cu(NO_3)_2$) and silver nitrate ($AgNO_3$) metal salt precursors, dispersed in deionised water at Ag/Cu ratios of 0/100, 1/99, 3/97, 8/92, and 25/75 by weight, referred to throughout the text as 0, 1, 3, 8 and 25 wt% Ag. The metal salt solution was fed upwards into a counter-current nozzle reactor, where it mixed with a 250 °C downflow solution of sodium hypophosphite ($NaPO_2H_2$) in water. The flowrate of both streams was set at 20 mL $min^{-1}$, and the system pressure was maintained at 172 bar. Following synthesis, the nanoparticles were washed and redispersed in a propan-2-ol solvent with 5 g $L^{-1}$ lactic acid for bar coating. Energy dispersive X-ray (EDX) analysis of the final inks was performed in order to confirm the Ag weight loadings (see '*in situ* thermal sintering and nanoparticle imaging *via* SEM' section for instrument details). These data are provided in the SI Section S1.1.

**Laser diffraction analysis of Cu–Ag hybrid inks.** For laser diffraction analysis (LDA), the inks were diluted in propan-2-ol (purchased from Sigma Aldrich) to an obscuration level of approximately 15%. The ISO 13320:2009 (Particle Size Analysis – Laser Diffraction Methods) standard was followed, using the wet cell of a Malvern Mastersizer 3000, to determine particle size *via* laser diffraction.[83] The beam alternates between monochromatic red and blue lasers, and the light scattered by particles was measured using multi-element detectors at various angles for a total of 3.5 min for each sample.

**Nanoparticle ink deposition.** The NP inks were deposited using a bar coating technique (see SI Section S1.2). The inks were sonicated for 30 minutes in an ultrasonic bath prior to deposition. The inks were dispensed in excess from pipettes onto clamped glass substrates and manually spread using metal hand-coater bars, purchased from RK Print, until the substrate was covered, and the surplus had been removed. The dimensions of the resultant films were ~25 mm by ~55 mm and after deposition, the films were left to dry *via* evaporation, generally taking <30 s. The final film thickness was 7 ± 1 μm.

**Particle sintering of Cu–Ag hybrid inks.** Thermal sintering of the bar-coated Cu–Ag samples was performed in air using a laboratory hotplate and a thermocouple fixed to the sample surface using heat-resistant Kapton® tape. The temperature was increased incrementally from ambient conditions up to 265 °C in 10 °C steps. Each temperature was maintained for 2 minutes, with a sheet resistance reading taken at the end of this period. Each test was repeated at least three times. Low power laser irradiance was performed through a custom-built system, consisting of a fibre laser (BKtel GmbH, Hückelhoven, Germany) using ≤10 W at a wavelength of 1064 nm, a scan head (hurrySCAN, Scanlab GmbH, Puchheim, Germany), a 164 mm T-theta lens, and control software (laserDESK, Scanlab GmbH, Puchheim, Germany). A 2.5 W laser power and 150 mm $s^{-1}$ laser scan rate was used, with the laser operated in continuous wave mode. The hatch distance between the parallel laser scan lines was 50 μm. The laser beam profile was Gaussian in shape with a 32 μm 90/10 knife edge in the *x* and *y*-directions. Laser irradiation of the NPs was carried out under ambient conditions.

 

A Heraeus Noblelight flash lamp system was used for IPL sintering. Samples were placed under the flashlight, with a distance of 15 mm maintained between the bottom of the lamp and the surface of the sample. Samples were exposed to a single flash, with a duration of 6 ms, at a voltage of 400 V. Sheet resistance measurements were performed to determine the impact of Ag addition to the Cu NPs on the electrical resistance under the various sintering techniques employed *via* a four-point probe (Measuring Device Type SD-800, Measuring Probe Type SDKR-13, NAGY Messsysteme GmbH, Gäufelden, Germany).

**X-ray diffraction (XRD) analysis of Cu–Ag hybrid inks.** A Bruker D8 Advance Da Vinci XRD system (Bruker Corp. MA, USA) with Cu Kα radiation was used for XRD analysis, with 35 mm × 35 mm samples studied. XRD patterns were collected over a $2\theta$ range of 10–100° with a step size of 0.02° and counting time of 74.5 s. Mean crystallite size was quantified before and after sintering using the Scherrer Equation.[84] The peak shapes were assumed to be Gaussian and peak broadening due to micro strain was assumed to be negligible. The instrument broadening was measured using a bulk Cu reference sample. The Kα2 contribution to scans was subtracted prior to all peak width measurements.

**Differential scanning calorimetry (DSC) of Cu–Ag hybrid inks.** DSC analysis was performed using a TA Q600 (TA Instruments, NC Delaware USA). The sample ink was placed into an alumina pan and heated at a temperature ramp rate of 10 °C $min^{-1}$ under a constant 100 mL $min^{-1}$ nitrogen flow to prevent oxidation. The DSC data for Cu NPs is provided in the SI Section S1.3.

***In situ* thermal sintering and nanoparticle imaging *via* SEM.** To study NP sintering behaviour in real time, a Field Emission Gun Scanning Electron Microscope (FEG-SEM) JEOL 7100F FE-SEM (JEOL Ltd. Akishima, Tokyo, Japan) was fitted with a Gatan Murano 525 *in situ* heating stage. The transferable carriage assembly was coupled with mating electrical contact pins for a heater and a temperature sensor. Samples were mounted onto consumable silicon hotplates, located on ceramic block supports. A power booster provided power up to 20 W, while the temperature of the hotplate was determined by a USB temperature controller. Cooling was enabled *via* a recirculating water system. The hot plate was covered by a metallic shield with a 2 mm sized circular aperture, to protect the components inside the SEM from light emission and radiative heating effects, whilst still enabling imaging of the specimen surface. The temperature of the heating stage was increased in 30 °C increments and held at each value for 10 minutes. Images were captured using the secondary electron detector at each temperature increment over a 5-minute period. The FEG-SEM used an in-lens Schottky field emission source with an integrated Oxford Instruments X Max silicon drift detector for EDX analysis. It was operated at 15 keV and the sample was maintained at a working distance of 12.5 mm. Details regarding the analysis of the SEM images can be found in the SI Sections S1.4 and S1.5.

# Results

### Characterisation of Cu–Ag hybrid inks

As-produced Cu–Ag dispersions were characterised using XRD to investigate and confirm the presence of both materials within the inks. XRD patterns for inks with 1, 3, 8 and 25 wt% Ag, with respect to the total metal content according to the precursors used within the synthesis protocol, are shown in Fig. 2a. It can be seen that with increasing Ag precursor concentration, the intensities of the characteristic Ag peaks within the XRD patterns increase, at the expense of the characteristic Cu peaks, which are seen to decrease in intensity; the intensity ratio between the strongest Ag reflection and the strongest Cu reflection (at $2\theta$ angles of ~38.1° and 43.3° respectively, corresponding to the {111} planes) increases from $I_{Ag111}/I_{Cu111}$ ~0.02 for the 1 wt% Ag ink to 0.04, 0.06, and 0.34 for the 3, 8 and 25 wt% Ag inks. SEM/EDX analysis (SI Section S1.1) verifies that the final inks contain on average 1, 3, 8 and 25 wt% Ag with respect to the total metal content (Ag + Cu). In addition, no peak shifting indicative of alloy formation[55,62] is observed for either Cu or Ag in Fig. 2a, supporting that the hybrid inks are simple mixtures of discrete metallic Cu and Ag NPs.

Fig. 2b shows the results of laser diffraction analysis, demonstrating the impact of Ag addition on the particle sizes within the Cu–Ag inks. Fig. 2b is a semi-log plot of particle diameter against cumulative particle volume, in which the majority of the volumetric particle distribution is represented by the linear section of the curve with the largest gradient. For all inks, it can be seen that the size distribution is relatively broad, with particles ranging from below 100 nm to several microns in diameter. With increasing Ag content, the steep linear section of each curve shifts to the left, indicating a decrease in average particle diameter with increasing overall Ag weight loading; this is a result of the smaller size of the Ag particles with respect to the Cu particles, as made clear *via* the SEM images (Fig. 6 and 7) and discussed in the related section.

### Sheet resistance of Cu–Ag films sintered *via* different approaches

Following characterisation of the inks, Cu–Ag films were deposited *via* bar-coating onto glass slide substrates, as depicted in the schematic diagram in Fig. 1 and the image in Fig. S5 of the SI. Bar coated Cu–Ag films with varying Ag weight loadings were post-processed using a traditional thermal sintering method, along with ultrafast laser-based and intense pulsed light sintering techniques. A schematic diagram depicting each of these approaches is further shown in Fig. 1 and a photograph of a representative sintered bar coated sample is given in Fig. 3a. The sheet resistances of bar coated Cu–Ag films under thermal, laser, and IPL sintering are given in Fig. 3b–d. For thermally sintered samples, sheet resistance measurements were taken at regular temperature intervals.

The Cu–Ag NP samples containing 0 and 1 wt% Ag did not show any measurable electrical conductivity following thermal sintering in air; therefore, those samples are not represented in Fig. 3b. However, the films containing 3, 8, and 25 wt% Ag showed measurable electrical conductivity, with the sheet resistance in each case decreasing with increasing sintering temperature. No clear trend is observed between the Ag weight loading and the sheet resistance of the bar coated films processed *via* laser sintering (Fig. 3c). However, it should be

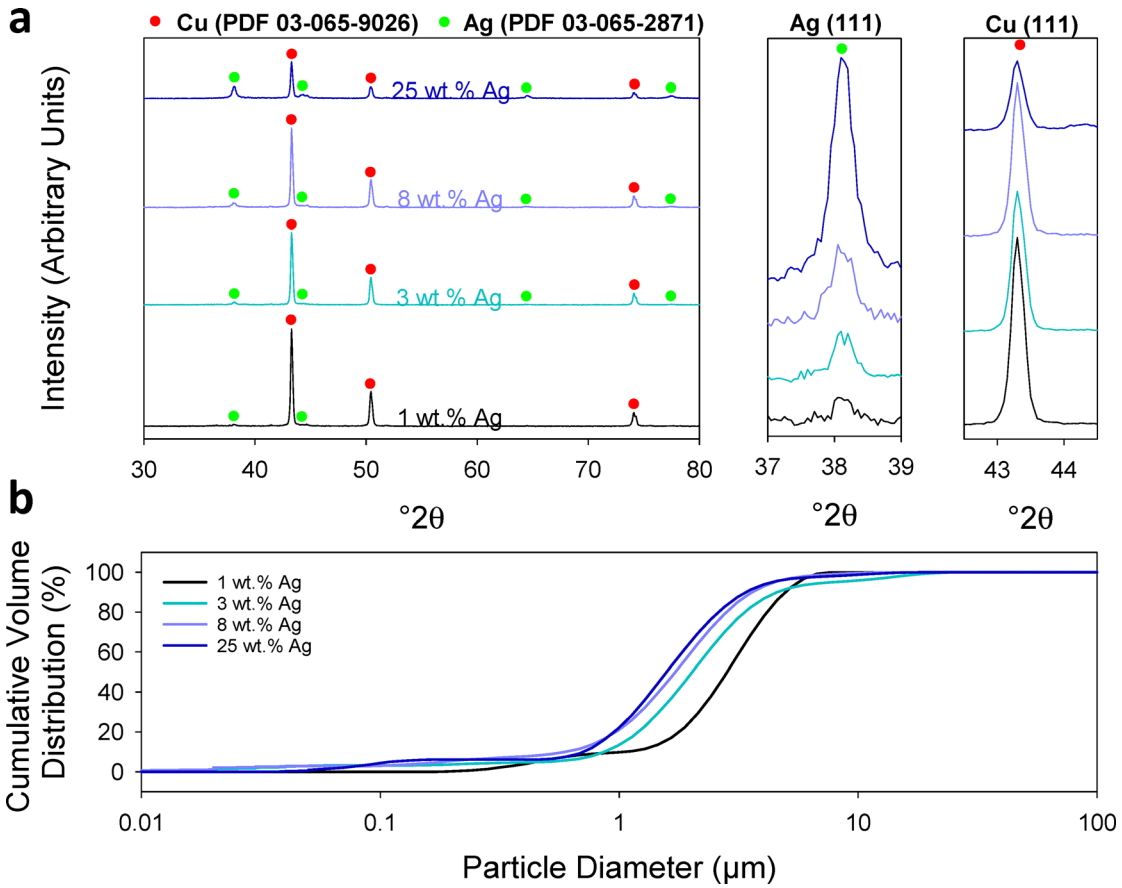


Fig. 2 (a) XRD patterns for NP inks with varying Ag/Cu mass ratios. Positions for the characteristic Ag and Cu peaks are indicated by green and red circles respectively. Inset: Zoomed view focusing on the strongest {111} Ag and Cu reflections. (b) LDA analysis showing particle size distribution of Cu inks with varying Ag weight content.

noted that all samples demonstrated measurable electrical conductivity, including the Cu-only sample with 0 wt% Ag. Similar results are shown in Fig. 3d for IPL sintered samples; again, no clear trend is observed but all samples demonstrate relatively high levels of conductivity. This is in contrast to the sheet resistance of thermally sintered samples (Fig. 3b). Between the photonic sintering techniques, the IPL processed materials demonstrated the lowest overall sheet resistance values compared with the laser sintered samples, regardless of Ag weight loading. This disparity could be due to differences in homogeneity between IPL and laser sintered samples as a result of their differing irradiation mechanisms. During laser sintering, a spatially confined 32 μm laser spot moves across the sample in parallel line scans with a hatching distance of 50 μm, as opposed to IPL sintering, in which the light pulse irradiates the entire sample simultaneously.

## Discussion

### Thermal sintering of Cu–Ag hybrid ink in an air environment

For a given sintering temperature, the sheet resistance of a Cu–Ag hybrid film decreases with increasing Ag content, for Ag weight loadings of $\geq$3%, with values as low as $\sim$1 Ω sq$^{-1}$ obtainable for Cu–Ag films containing 25 wt% Ag (Fig. 3b). Visual observation of a Cu-only sample during the thermal treatment in air indicated a distinctive colour change from the typical Cu dark red to a bluish grey, commonly associated with insulating copper oxides, from temperatures of above $\sim$90 °C. DSC measurements show that sintering of the Cu NPs begins at $\sim$155 °C and becomes significant at temperatures above $\sim$260 °C (see SI Section S1.3 and Fig. S6). Thus, it appears that Cu NPs subjected to increased temperatures in an ambient environment begin to oxidise before they can sinter. This is further supported by the data in Fig. 4, which shows the XRD patterns for Cu–Ag films, with varying Ag loadings, both before and after thermal sintering at 265 °C in air.

Using the Scherrer equation,[84] an average increase in mean Ag crystallite size of 117% was observed between unsintered and thermally sintered samples containing 25 wt% Ag (from 29 nm to 63 nm). This Ag grain growth is a strong indication that Ag sintering has indeed occurred. However, whilst characteristic Cu peaks may still be observed in the XRD pattern of the sintered 25 wt% Ag samples, it is clear when comparing Fig. 4a and b that significant oxidation has arisen as a result of thermal treatment, with peaks for copper oxide also present. The XRD patterns for Cu–Ag materials containing 0, 1, 3, and 8 wt% Ag indicate complete Cu oxidation after the thermal treatment in an air environment (Fig. 4b), with no characteristic Cu peak remaining

 

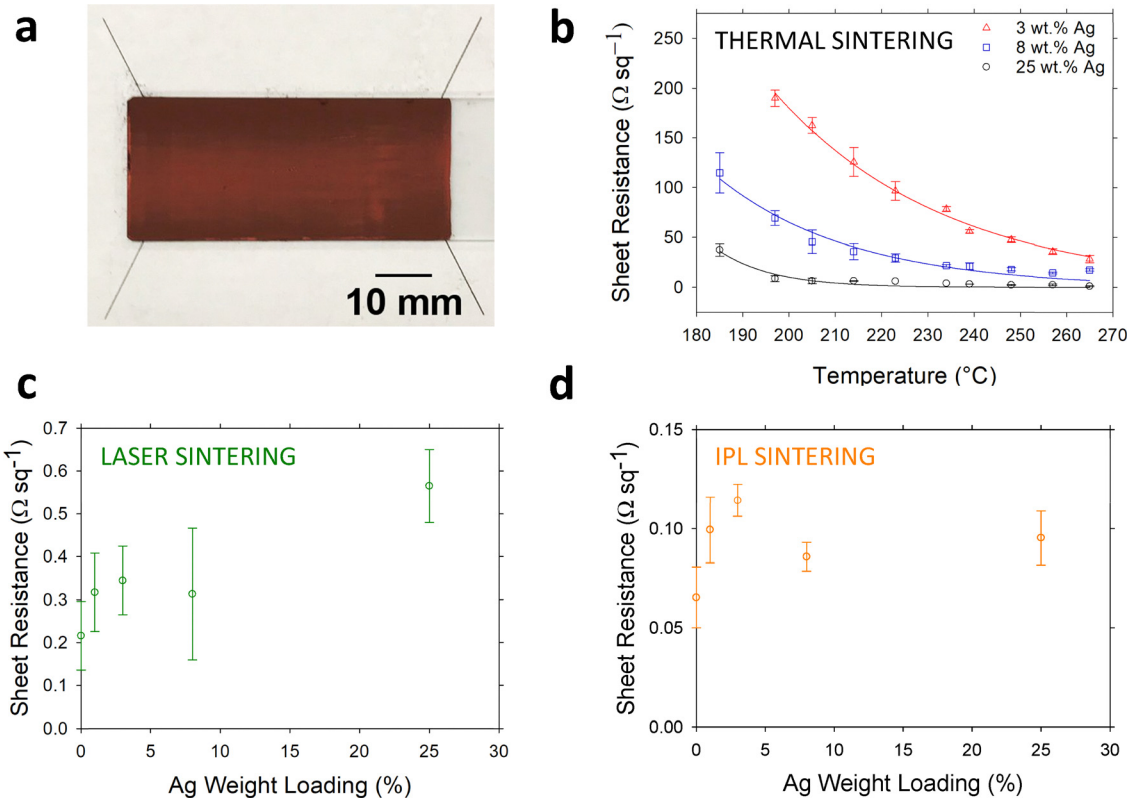


Fig. 3 (a) Photograph showing sintered ink on a glass slide substrate. (b) A comparison of sheet resistance values obtained with varying thermal sintering temperatures for Cu inks with differing Ag weight contents. Variation in sheet resistance with Ag weight loading for bar-coated Cu–Ag inks under laser (c) and IPL sintering (d). Each test was repeated at least three times.

in the post-processed samples. This suggests that only the highest Ag content tested (25 wt%), was the silver able to provide some degree of protection, acting as a barrier to the surrounding air and preventing complete Cu oxidation, as described in the reports of Cu–Ag core–shell materials.[41,60,61,85,86] This, in turn, may also enable the Cu particles to begin sintering, leading to increased electrical conductivity within the films. However, as shown in Fig. 3b, the hybrid films containing 3 and 8 wt% Ag demonstrated measurable conductivity following the thermal sintering in air, despite the complete oxidation of the Cu content, as indicated by the XRD. This suggests that the conductivity in the final samples stems mostly from the Ag, and not from possible sintering of the Cu; rather than acting to prevent oxidation, the Ag is instead forming a continuous conductive network, around the CuO particles, as previously reported,[53,60] and as supported by the measured Ag grain growth.

### Thermal sintering of Cu–Ag hybrid ink in a low-air environment

In order to investigate the thermal sintering phenomenon further, *in situ* heat treatment of Cu NP and Ag NP samples was performed under vacuum inside an FEG-SEM, with images taken at regular temperature intervals. Oxidation impacts the mass transport phenomena involved in particle sintering, as it chemically changes the composition of the material. The absence of oxygen therefore allows analysis of the elemental metal NP sintering process without any oxidation occurring.

Fig. 5 shows SEM images of a Cu NP cluster taken *in situ* during thermal sintering. The advantage of using such a method is that the very same group of particles may be monitored throughout the entire temperature ramp, with specific changes identified and tracked. It can be seen that, as the sintering temperature increases, the smaller individual Cu particles fuse together to create larger particles. This coarsening appears particularly evident at temperatures >350 °C, suggesting that this is the onset point for significant Cu particle sintering.

This further supports that the copper nanoparticles within the hybrid inks will begin to oxidise (Fig. 4) at temperatures lower than that required for substantial sintering to occur. Additional analysis of the Cu NPs during sintering is provided in the SI Section S1.6. A selection of representative secondary electron SEM images for Ag-only NPs taken at various temperature intervals during the sintering process are given Fig. 6a–d. Particle sintering for the Ag NPs is noticeably different to that of the Cu NPs. Ag sintering begins at lower temperatures and appears to proceed according to a different mass transport phenomenon; where Cu NPs undergo particle fusion, during which entire smaller particles fuse into adjacent larger particles, Ag NPs appear to predominantly form 'necks'. Image analysis was performed in order to further characterise the Ag NP sintering process (see SI Section S1.4 for details). The number of Ag NPs which sintered during the thermal treatment

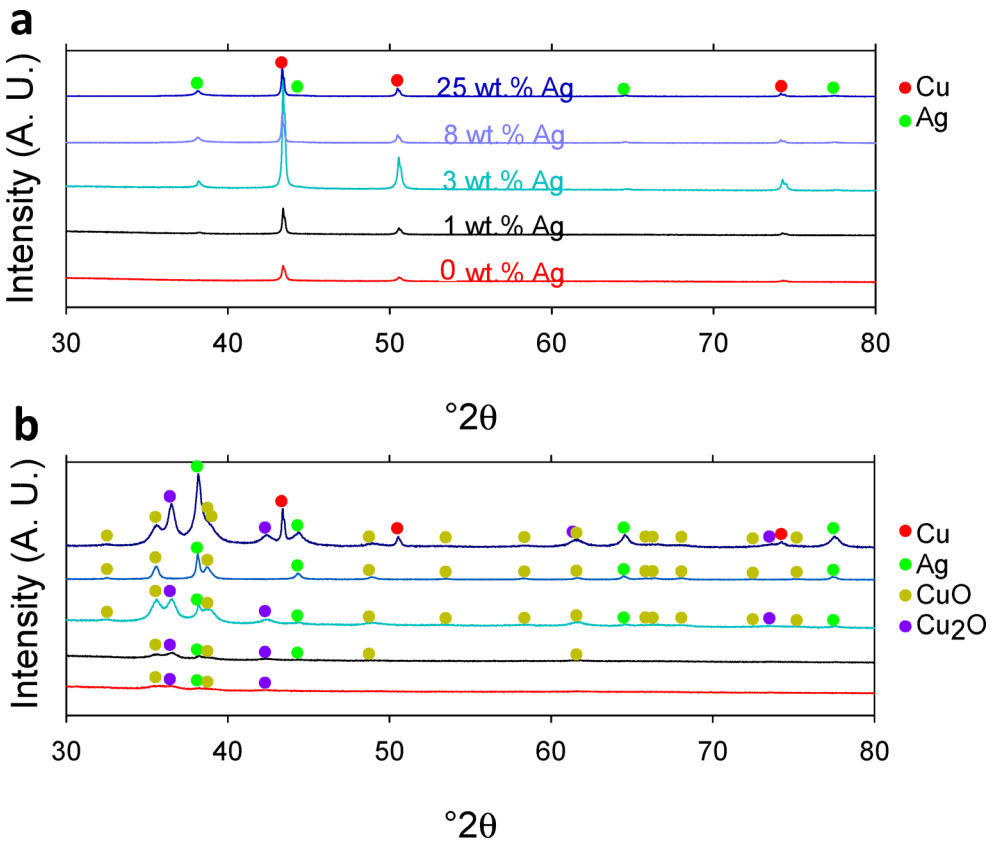


Fig. 4 XRD patterns for Cu–Ag NP bar coated samples with varying Ag mass loadings before (a) and after (b) thermal sintering at 265 °C under ambient conditions. Peak positions for characteristic Ag (Green Circles, PDF 03-065-2871) and Cu peaks (Red Circles, PDF 03-065-9026), along with copper oxides (Yellow Circles CuO, PDF 01-073-6023 and Purple Circles $Cu_2O$, PDF 01-071-3645), are shown by the accompanying ticks.

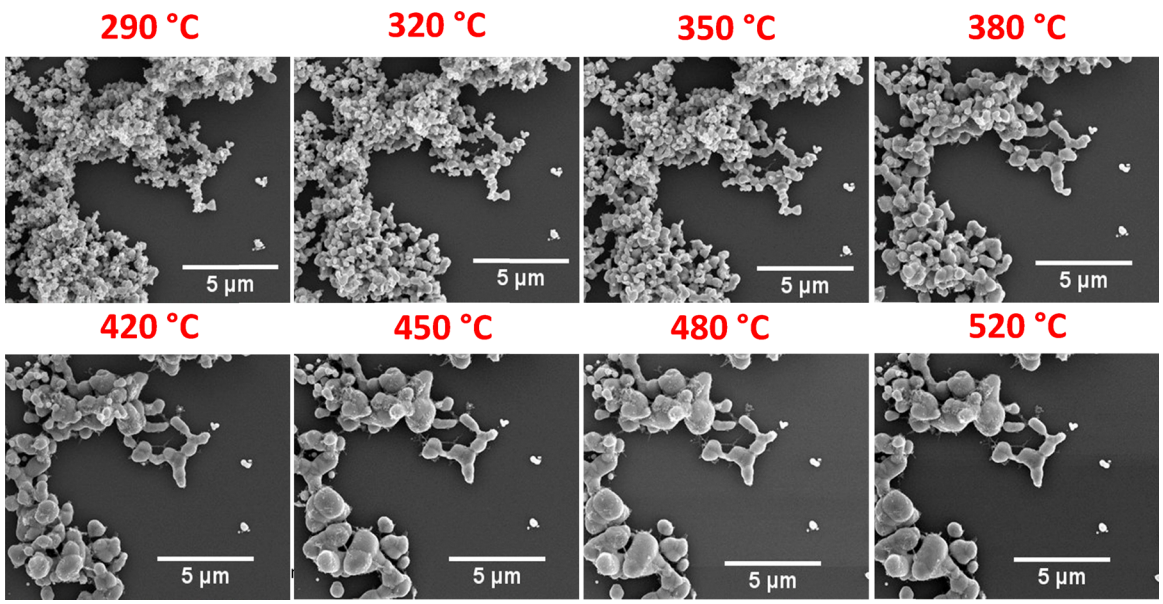


Fig. 5 Secondary electron SEM images of Cu NPs acquired *in situ* from the same location at various temperature intervals, indicated by the red labels.

as a fraction of the total number of initially unsintered Ag NPs is plotted against the sintering temperature in Fig. 6e. There is a sharp increase in the number of particles sintered between 100 and 200 °C, with the highest rate of neck formation observed between 170 and 200 °C. This neck formation is the consequence of enabled mass transport of the Ag NPs.

 

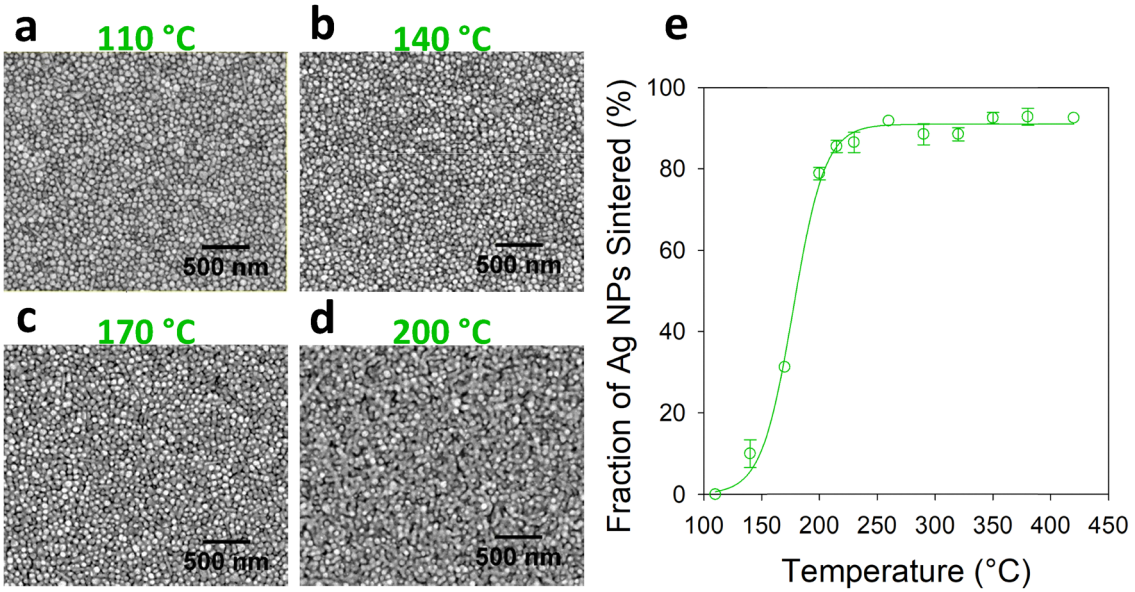


Fig. 6 Secondary electron SEM images of Ag NPs captured at (a) 110 °C, (b) 140 °C, (c) 170 °C and (d) 200 °C. (e) The progression of Ag NP sintering with increasing temperature, determined *via* SEM image analysis.

The 170–200 °C Ag sintering temperature range determined from the SEM image analysis is consistent with the 150–250 °C temperature limit stated within the majority of literature reports as the onset point for Ag shell de-wetting from Cu NP cores.[46–49,52–59] It should also be noted that the electrical resistance of the Cu–Ag hybrid materials with 3, 8 and 25 wt% Ag content was too high to be measured after sintering at temperatures below 185 °C, with measurable electrical conductivity obtained only at higher temperatures (Fig. 2b). Therefore, during thermal sintering, tangible conductivity is realised for Cu–Ag films at a temperature consistent with the range at which the Ag NPs were found to be most mobile (170–200 °C). This further supports Ag mobilisation and network formation as the mechanism by which conductivity is obtained, as opposed to the prevention of Cu oxidation by Ag NPs during thermal treatment in air. Ag NP network formation was further studied within the composite samples *via* backscattered electron images taken from the 25 wt% Cu–Ag hybrid film following *in situ* thermal sintering within the FEG-SEM, with EDX spectra additionally acquired and overlaid. Representative SEM images are shown in Fig. 7a and c, with the EDX data provided in Fig. 7b and d, for isolated particles and coated regions respectively. SEM images obtained using the backscatter detector are informed by high-energy electrons which are reflected, or back-scattered, out of the specimen volume *via* elastic interactions with specimen atoms. Since heavy elements backscatter electrons more strongly than lighter elements, the heavy elements appear brighter in colour within backscatter electron images. It therefore follows that the brighter regions within Fig. 7a and c represent Ag (Atomic Number, $Z$ = 47), and the darker regions represent Cu ($Z$ = 29). To investigate the distribution of Ag with respect to Cu, the EDX map spectra were obtained and overlaid with the backscatter electron images. These EDX scans confirm that the lighter areas within the SEM images are indeed regions of high Ag concentration, whilst the darker areas are regions of high Cu concentration. EDX point spectra were also obtained, with the locations indicated by markers in Fig. 7b and d. The Cu/Ag weight ratios in the regions from which the point spectra were taken have been calculated. These ratios are provided in Table 1. From the backscatter electron images and the corresponding EDX data, it is possible to see that a large fraction of the Ag is located in the necking regions of Cu particles. The lower melting point (and therefore lower cohesive energy) of Ag, with respect to Cu,[87] leads to Ag becoming mobile at lower temperatures. With this increased mobility, the Ag migration is strongly influenced by the effects of surface tension. As Ag has a lower surface tension than Cu (0.89 N m$^{-2}$ for Ag[88] and 1.31 N m$^{-2}$ for Cu[89]), it follows that Ag wets the Cu surface,[88–90] accumulating within the necking regions between two adjacent Cu particles, as the Ag–Cu interface is energetically more favourable than the interface between the Ag and the surrounding air. The accumulation of Ag in the necks of Cu NPs increases the contact area between adjacent particles and thereby enhances the electrical conductivity of the system. The data provided in Fig. 2–7 indicate that from a threshold level of as low as 3 wt% Ag within a Cu–Ag hybrid film, sufficient Ag is present to enable the formation of a connected conductive network upon mobilisation at increased thermal sintering temperatures. It follows that this energetically favourable re-distribution of Ag over the Cu during the thermal sintering process may mitigate future electromigration issues associated with Ag NP use; indeed, many studies have demonstrated that combined Cu–Ag systems show improved electromigration resistance with respect to Ag alone.[91–95] Theoretical calculations were performed to see how this phenomenon of Ag network formation could be optimised *i.e.*, obtaining maximum

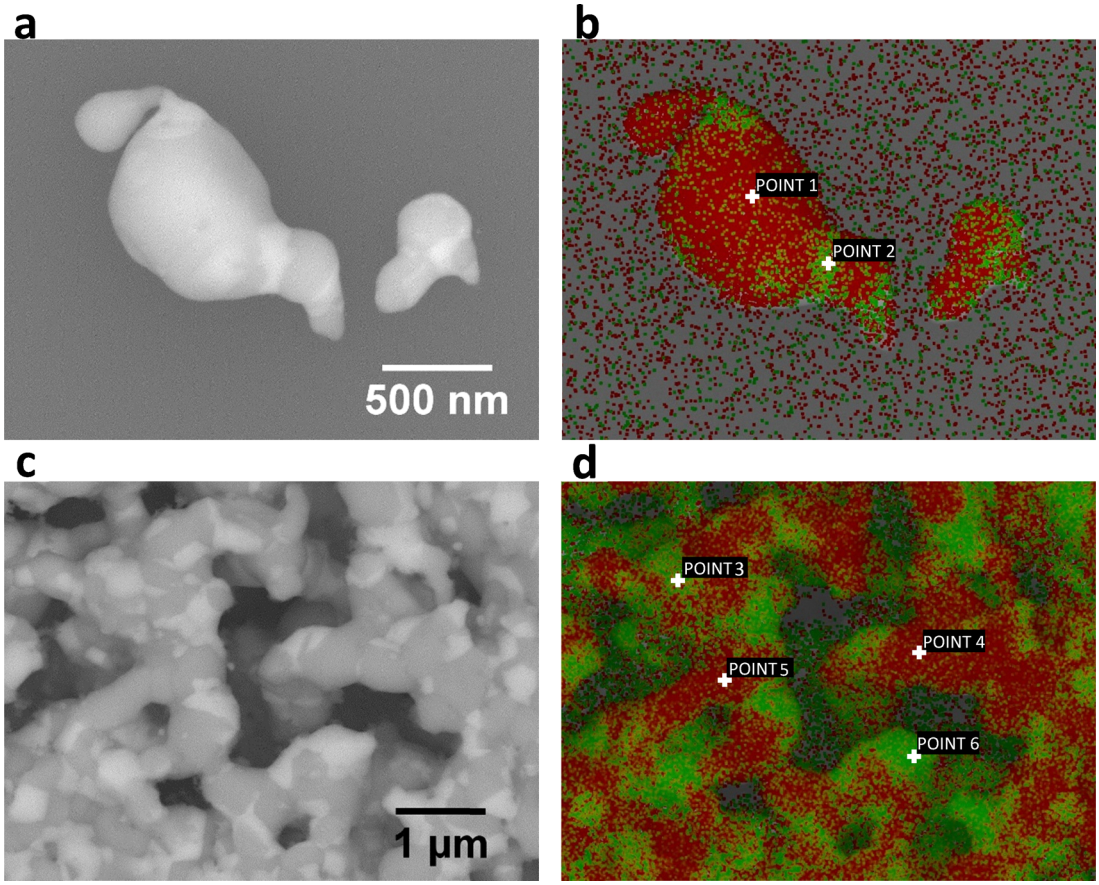


Fig. 7 Backscattered electron SEM images (a) and (c) and the same images overlaid with EDX scans (b) and (d) for isolated Cu–Ag particles and coated regions respectively, taken from the 25 wt% hybrid film, where red areas represent Cu and green areas represent Ag. EDX point spectra were taken from images (b) and (d) as indicated by the markers.

Table 1 Cu/Ag weight ratios from point spectra taken in areas 1–6, indicated by markers shown in Fig. 7b and d

| Point spectra | Cu/Ag weight ratio |
|---|---|
| 1 | 10.5 |
| 2 | 0.8 |
| 3 | 0.3 |
| 4 | 6.4 |
| 5 | 6.6 |
| 6 | 0.1 |

electrical conductivity through the minimum addition of silver. No similar simulations were found within the literature. Details regarding the computational modelling, including the assumptions made and the MATLAB script utilised, can be found in Section S1.7 of the SI. Three different independent variables were investigated: the Ag/Cu mass ratio, the Cu–Cu neck size, and the Cu/Cu adjacent particle size ratio. A schematic diagram depicting Ag accumulation in the necking region between two Cu particles of equal size, along with the corresponding resistance reduction simulation data, are provided in Fig. 8a and c, respectively. As seen in Fig. 8a, two adjacent Cu particles of equal diameter have been considered, with a neck formation between one tenth to one third of the Cu particle diameter in size, with Ag filling this neck up to half of the diameter of the Cu particle. It can be seen from Fig. 8c that in every case, increasing the Ag/Cu weight ratio decreases the overall resistance of the system with respect to Cu-only. However, an increased degree of prior neck formation between the two Cu particles lessens the effect of the Ag addition: the larger the Cu–Cu neck, the smaller the increase in conductivity due to the associated Ag accumulation. These trends are independent of varying particle size, provided that the sizes of the two adjacent Cu particles are equal. Thus, in order to best utilise the concept of Ag accumulation in the Cu particle necks, the chosen temperature for heat treatment during post-processing should be higher than that required for the Ag to become mobile, yet low enough to prevent the Cu NPs sintering to a high degree of densification. This would minimise the size of the Cu particle necks and hence maximise the impact of Ag accumulation. As discussed, the Ag content of the system seems to become most mobile within the temperature range of 170–200 °C (see Fig. 6), whilst the fusion of adjacent Cu particles seems to proceed at higher temperatures (see Fig. 5 and SI Section S1.6). A sintering temperature >200 °C but <350 °C may therefore be most appropriate for the thermal treatment of Cu–Ag hybrid inks. For adjacent Cu particles of varying size, neck formations between one eighth to one quarter of the larger Cu particle diameter were considered, with Ag filling the neck up to one third of the larger Cu particle diameter. A schematic diagram depicting this scenario,

 

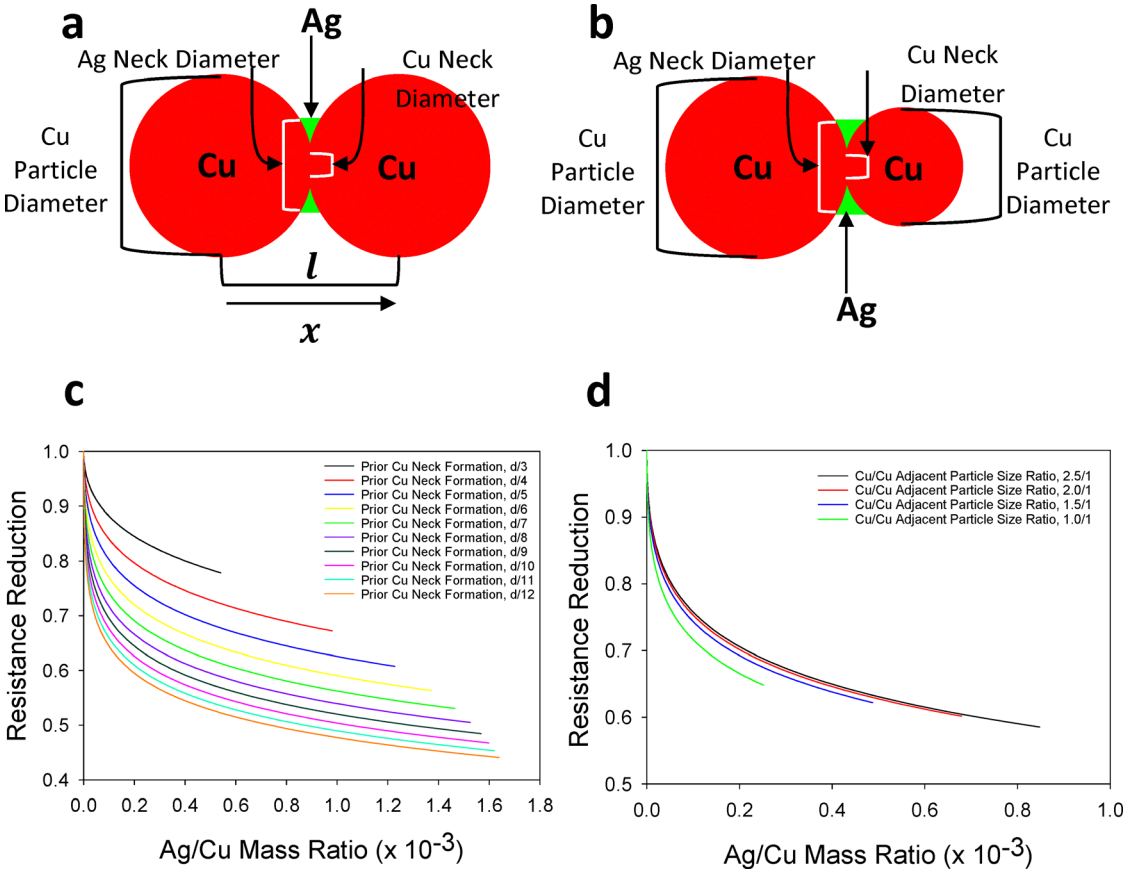


Fig. 8 Illustrations showing Ag accumulation in the necking region of two adjacent sintered Cu particles of (a) equal diameter and (b) differing diameters. The overall length of the object is given by *l* whilst *x* indicates the one-dimensional spatial position along the sintered object. (c) Theoretical resistance reduction between two Cu particles of equal size due to Ag accumulation in the Cu necking area with increasing Ag/Cu mass ratio. Each curve ends when an Ag neck filling of *d*/2 is reached. The Cu particle diameter is denoted as '*d*'. (d) Theoretical resistance reduction between two Cu particles of differing sizes due to Ag accumulation in the Cu necking area with increasing Ag/Cu mass ratio for a Cu–Cu neck size of *d*/8, where *d* refers to the diameter of the larger Cu particle. Each curve ends when a maximum Ag neck filling of *d*/3 is reached.

along with resistance reduction simulation data for a prior Cu–Cu neck formation of *d*/8 (where '*d*' is the diameter of the larger Cu particle), are provided in Fig. 8b and d, respectively. Similar data for prior Cu–Cu neck formations of *d*/4 and *d*/6 are provided in the SI (Section S1.7.3), with the same trend observed as for Cu particles of equal diameter; the smaller the Cu–Cu neck, the larger the improvement in conductivity. It can be seen from Fig. 8d that for a constant Cu–Cu prior neck size, an increasing Cu/Cu adjacent particle size ratio lessens the reduction in inter-particle electrical resistance due to the Ag accumulation in the neck, for a given Ag weight loading. A wide particle size distribution amongst the Cu NPs would increase the probability of adjacent particles significantly differing in diameter. It therefore follows that, in addition to careful selection of the sintering temperature to minimise prior Cu neck formation, a Cu NP particle system with a relatively narrow size distribution is desirable for maximising the reduction of resistance in the final Cu–Ag film upon Ag NP addition.

### Light-based sintering of Cu–Ag hybrid inks

It was observed that all bar-coated Cu–Ag films, across all Ag weight loadings, demonstrated measurable conductivity following laser and IPL sintering. XRD patterns for samples post-processed *via* the laser and IPL techniques, compared with unsintered, as-deposited samples, are shown in Fig. 9. Copper oxide peaks are absent from both the laser- and IPL-treated patterns, with very little change observed in the post-processed XRD data. When coupled with the sheet resistance data, this indicates that oxidation within the final films may be avoided through the use of light-based sintering techniques. This is consistent with other literature reports in which Cu NPs have been post-processed using laser and IPL treatments.[69,75] The absence of any clear correlation between the sheet resistance and the Ag weight loading of the Cu–Ag films (Fig. 3c and d) suggests that the addition of Ag NPs to Cu NPs has no significant impact on the electrical properties when laser and IPL sintering methods are utilised. Typically, the activation energy required for particle sintering decreases with decreasing particle diameter (SI Section S1.6). Although LDA analysis (Fig. 2b) did indicate a decrease in the overall particle size distribution of the Cu–Ag hybrid inks with increasing Ag content, the distribution itself remained broad in each case. Furthermore, bulk Cu resistivity is only 5.6% greater than the resistivity of Ag. Thus, in the absence of Cu oxidation, the effects of the reduced particle size and increased conductivity of the Ag NPs are minimal, with the conductivity of the final hybrid samples most likely

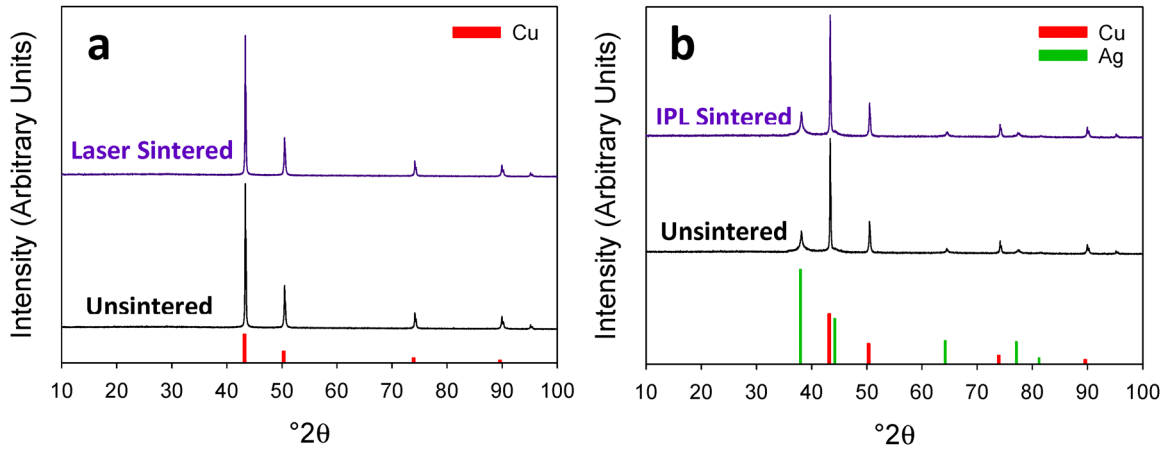


Fig. 9 (a) XRD patterns of Cu NPs before (bottom) and after (top) laser sintering and (b) XRD patterns of Cu–Ag NPs before (bottom) and after (top) IPL sintering. Characteristic Cu and Ag peaks are indicated in red and green, respectively. No additional peaks relating to copper oxides are observed.

Table 2 Comparison of electrical performances for state-of-the-art Cu–Ag hybrid inks; in cases where either sheet resistance or resistivity was stated, the other value was, where possible, calculated using film thickness data, where provided

| Cu–Ag system type | Sheet resistance ($\Omega$ sq$^{-1}$) | Ink production method | Sintering procedure | Study |
|---|---|---|---|---|
| Cu–Ag hybrid ink 3 : 1 Cu to Ag ratio | 1.330 ($\rho$ = 9.310 × $10^{-4}$ $\Omega$ cm$^{-1}$) | Single-stage, continuous flow, simultaneous synthesis of Cu and Ag NPs. | In air, 265 °C, ~60 minutes | This work |
| Cu & nano-Ag blended ink 3 : 1 Cu to Ag ratio | ~0.700 ($\rho$ ~ 1.750 × $10^{-5}$ $\Omega$ cm$^{-1}$) | Manual mixing of commercial Cu micro-particle and Ag NP inks. | Under hydrogen-nitrogen 250–275 °C, 40 minutes | 68 |
| Ag-coated Cu μ-particles 1 : 1 Cu to Ag ratio | 0.326 ($\rho$ = 3.260 × $10^{-4}$ $\Omega$ cm$^{-1}$) | Cu particle synthesis followed by Ag coating, both batch processes. | Under reducing atmosphere 200 °C, 60 minutes | 97 |
| Thick-shell Cu@Ag–nano-rod surface morphology 9 : 1 Cu to Ag ratio | None provided. (film thickness unknown) ($\rho$ = 7.144 × $10^{-5}$ $\Omega$ cm$^{-1}$) | Cu particle synthesis under $N_2$, followed by Ag seed layer growth, also under $N_2$, and later thick Ag shell formation—all batch. | In air, 160 °C, 30 minutes | 98 |
| Cu@Ag core–shell NPs 3 : 1 Cu to Ag ratio | 0.013 no film thickness or resistivity provided | Multi-stage batch synthesis; several precursor preparation steps, then Cu NP synthesis & subsequent Ag shell formation. | Assumed air (not specified) 170 °C, 20 minutes | 99 |
| Cu@Ag core–shell NPs 2 : 1 Cu to Ag ratio | 0.210 ($\rho$ = 3.922 × $10^{-4}$ $\Omega$ cm$^{-1}$) | Cu NP synthesis, then Ag encapsulation—both batch processes. | In air, 250 °C, 3 0 minutes | 100 |
| Particle-free Ag-Cu hybrid metal–organic decomposition ink 1.05 : 1 Cu to Ag ratio | 11.342 (assuming single layer, thickness of 2.14 μm) ($\rho$ = 2.427 × $10^{-3}$ $\Omega$ cm$^{-1}$) | Separate, batch syntheses of Cu & Ag metal–organic precursor inks which are then mixed; metal NPs formed on sintering – decomposition of organic complexes. | In air, 135 °C, 60 minutes | 101 |

a result of successful Cu NP sintering. Indeed, the average Cu crystallite size following laser sintering was 433 ± 73 nm, as determined through the Scherrer equation, compared to a 315 ± 54 nm crystallite size measured prior to laser sintering. It follows that in cases of light-based post-processing, the addition of Ag NPs is superfluous and indeed, would constitute an unnecessary expense in terms of raw material costs *i.e.* the price of Ag is approximately 75 times greater than that of Cu.[96] This is in contrast to thermally sintered Cu–Ag hybrids, where an increased Ag content led to improved conductivity in the final samples. Since many printed electronic industrial production lines are equipped with technologies designed for the more traditional thermal sintering procedures, the use of Cu–Ag hybrid inks may be one way to reduce the cost of depositing conductive features whilst obtaining viable sheet resistance values. The electrical performance of the thermally-sintered hybrid inks is compared with sheet resistance data for state-of-the-art Cu–Ag systems (reported in literature within the last two years) in Table 2. It can be seen that the resistance values obtained here are competitive with those in current reports, where most studies are still focused on core–shell structures; the Cu–Ag hybrid inks developed within this work were produced *via* continuous hydrothermal synthesis, with the inclusion of Ag NPs facilitated by the simple introduction of an additional silver nitrate precursor to an existing copper nanoparticle synthesis protocol. The inherent scalability of the continuous hydrothermal method combined with the simultaneous synthesis of both Cu and Ag NPs (in a single step) offers significant advantages over the core–shell approach, which usually proceeds *via* at least two separate batch processes – initial Cu NP synthesis and subsequent formation of an Ag shell. Other facile ink production approaches, such as the simple blending of two commercially-available Cu and Ag dispersions,[68] typically

 

require inert sintering atmospheres to obtain their notable resistivity values, whilst in this study, a simple hot plate in air was utilised for ink post-processing.

## Conclusions

In this work, hybrid Cu–Ag NP dispersions with differing Ag weight loadings were synthesised in a single, scalable step using a continuous hydrothermal method. Following formulation into a stable ink, the materials were deposited *via* bar-coating and post-processed through thermal, laser, and IPL sintering techniques. Cu oxidation was avoided through the rapid heating and cooling associated with light-based sintering, without the need for Ag addition. With light-based sintering, the addition of Ag particles was superfluous and conferred no significant conductivity improvement when compared with Cu only ink. Thermal sintering, in an oxygen-containing environment, resulted in Cu oxidation, although the addition of Ag, even at 3 wt%, led to significant reductions in the electrical resistance of post-processed samples. *In situ* monitoring of individual Cu and Ag particle clusters during thermal treatment (in an inert atmosphere *via* a novel SEM technique) showed that Ag NPs became mobile at significantly lower temperatures in comparison to those at which Cu NP sintering occurs. Hybrid samples containing 25 wt% Ag and 75 wt% Cu showed that mobilised Ag accumulated in the 'necks' found between adjacent Cu particles, forming a connected and conductive network. This finding explains observations made in previous reports around the impact of thermally sintering Cu–Ag core–shell particles, whereby Ag de-wets the Cu core at elevated temperatures in order to form such a network. As such, core–shell Cu–Ag structures do not appear necessary. The speed and scalability of the continuous hydrothermal synthesis approach, used within this work, offers noteworthy advantages over the core–shell approach, in which time and effort are dedicated to coating Cu NPs with a thin layer of Ag, only for it to mobilise and de-wet upon thermal treatment. For applications in which thermal sintering in an oxidising environment is preferred *e.g.* if available infrastructure does not provide for light-based post-processing or an oxygen-free sintering atmosphere (here, the samples were simply post-processed *via* hot plate), the addition of small amounts of Ag to Cu NPs can enable the achievement of sheet resistance values as low as $\sim 1\ \Omega\ \mathrm{sq}^{-1}$. Thus, the Cu–Ag hybrid inks proposed here are most competitive for use in large-scale printed electronics applications (due to the single-step, continuous-flow synthesis method) where sophisticated, inert-atmosphere post-processing equipment is unavailable. Theoretical simulations were used to optimise this phenomenon in which the Cu–Cu inter-particle resistance reduces due to Ag accumulation in the necking region. Results suggest that the maximum conductivity for the minimum Ag addition can be achieved through use of a Cu NP dispersion with a narrow particle size distribution, along with careful selection of the sintering temperature, in order to increase Ag mobility but decrease Cu neck formation. Further experiments are required to refine the synthesis parameters *e.g.*, reaction temperature, reaction pressure, flow rates and flow ratios, in order to reduce variations in Cu–Cu particle size, and to optimise the sintering procedure, in order to validate these predicted theoretical trends. Furthermore, studies surrounding the long-term stability of this Cu–Ag hybrid system, and any effects of further Ag electromigration, should be completed.

## Author contributions

Conceptualization, D. P., R. W. (Ricky Wildman), C. T. and R. H.; methodology, D. P. and E. L.; validation, R. W. (Ricky Wildman); formal analysis, D. P., R. W. (Robyn Worsley) and R. W. (Ricky Wildman); investigation, D. P. and R. W. (Ricky Wildman); resources, R. H.; data curation, R. W.; writing – original draft preparation, D. P., and R. W. (Robyn Worsley); writing – review and editing, A. B., C. T., R. H., R. W. (Robyn Worsley) and E. L.; visualization, R. W. (Robyn Worsley) and D. P.; supervision, R. H., R. W. (Ricky Wildman), C. T. and E. L. All authors have read and agreed to the published version of the manuscript.

## Conflicts of interest

There are no conflicts to declare.

## Data availability

The data supporting this article have been included as part of the supplementary information (SI). Supplementary information is available. See DOI: https://doi.org/10.1039/d5tc03927d.

## Acknowledgements

This work was funded by the Engineering and Physical Sciences Research Council Future Additive Manufacturing Platform Grant (EP/P027261/1) and the EPSRC Centre for Innovative Manufacturing in Additive Manufacturing grant (EP/I033335/2). The authors further acknowledge Promethean Particles Ltd. for their funding, with thanks to the team for supplying the materials used in this work and for allowing access to the Intense Pulse Flashlight (IPL). AB and RW acknowledge support for their time from the Intelligent Structures for Low Noise Environments Prosperity Partnership (EP/S03661X/1). The authors acknowledge access to facilities at the Centre for Additive Manufacturing (CfAM) within the University of Nottingham and would like to thank Mr Mark Hardy and Mr Mark East for their technical assistance in designing and developing the laser sintering system. We acknowledge access to facilities at the Nanoscale and Microscale Research Centre (nmRC) at the University of Nottingham and in particular the technical support from Mr Martin Roe with the host stage FEG-SEM.

## References


1 H. B. Lee, C. W. Bae, L. T. Duy, I. Y. Sohn, D. Il Kim, Y. J. Song, Y. J. Kim and N. E. Lee, *Adv. Mater.*, 2016, **28**, 3069–3077.
2 C.-W. Chen, H.-W. Kang, S.-Y. Hsiao, P.-F. Yang, K.-M. Chiang and H.-W. Lin, *Adv. Mater.*, 2014, **26**, 6647–6652.
3 S. Faraji and F. N. Ani, *Renewable Sustainable Energy Rev.*, 2015, **42**, 823–834.
4 A. Kamyshny and S. Magdassi, *Small*, 2014, **10**, 3515–3535.
5 V. Shrotriya, *Nat. Photonics*, 2009, **3**, 447–449.
6 M. Hilder, B. Winther-Jensen and N. B. Clark, *J. Power Sources*, 2009, **194**, 1135–1141.
7 C. C. Ho, K. Murata, D. A. Steingart, J. W. Evans and P. K. Wright, *J. Micromech. Microeng.*, 2008, **19**, 094013.
8 S. C. Chang, J. Liu, J. Bharathan, Y. Yang, J. Onohara and J. Kido, *Adv. Mater.*, 1999, **11**, 734–737.
9 A. A. Argun, P.-H. Aubert, B. C. Thompson, I. Schwendeman, C. L. Gaupp, J. Hwang, N. J. Pinto, D. B. Tanner, A. G. Macdiarmid and J. R. Reynolds, *Chem. Mater.*, 2004, **16**, 4401–4412.
10 Y. Yoshioka and G. E. Jabbour, *Synth. Met.*, 2006, **156**, 779–783.
11 S. Gamerith, A. Klug, H. Scheiber, U. Scherf, E. Moderegger and E. J. W. List, *Adv. Funct. Mater.*, 2007, **17**, 3111–3118.
12 D. Kim, S. Jeong, S. Lee, B. K. Park and J. Moon, *Thin Solid Films*, 2007, **515**, 7692–7696.
13 S. H. Ko, H. Pan, C. P. Grigoropoulos, C. K. Luscombe and J. M. J. Fr, *Nanotechnology*, 2007, **18**, 345202.
14 T. Sekitani, H. Nakajima, H. Maeda, T. Fukushima, T. Aida, K. Hata and T. Someya, *Nat. Mater.*, 2009, **8**, 494–499.
15 K. Song, D. Kim, X. S. Li, T. Jun, Y. Jeong and J. Moon, *J. Mater. Chem.*, 2009, **19**, 8881–8886.
16 V. R. Marinov, Y. A. Atanasov, A. Khan, D. Vaselaar, A. Halvorsen, D. L. Schulz and D. B. Chrisey, *IEEE Sens. J.*, 2007, **7**, 937–944.
17 F. Loffredo, G. Burrasca and L. Quercia, *Macromol. Symp.*, 2007, **247**, 357–363.
18 K. Chang, Y. H. Kim, Y. J. Kim and Y. J. Yoon, *Jpn. J. Appl. Phys., Part 1*, 2007, **43**, 7–8.
19 R. Möller, T. Schüler, S. Günther, M. R. Carlsohn, T. Munder and W. Fritzsche, *Appl. Microbiol. Biotechnol.*, 2008, **77**, 1181–1188.
20 J. B. Chang, V. Liu, V. Subramanian, K. Sivula, C. Luscombe, A. Murphy, J. Liu and J. M. J. Fréchet, *J. Appl. Phys.*, 2006, **100**, 14506.
21 V. Subramanian, J. M. J. Fréchet, P. C. Chang, D. C. Huang, J. B. Lee, S. E. Molesa, A. R. Murphy, D. R. Redinger and S. K. Volkman, *Proc. IEEE*, 2005, **93**, 1330–1338.
22 A. Ali, C. Smartt, J. Im, R. Mackenzie, O. Williams, E. Lester and S. Greedy, *Int. J. Microw. Wirel. Technol.*, 2022, 1–11, DOI: 10.2139/ssrn.3980406.
23 Z. Z. Fang and H. Wang, in *Sintering of Advanced Materials*, ed Z. Z. Fang, Woodhead Publishing, 2010, 434–473.
24 A. Kamyshny, J. Steinke and S. Magdassi, *Open Appl. Phys. J.*, 2011, **4**, 19–36.
25 J. Perelaer, B. J. De Gans and U. S. Schubert, *Adv. Mater.*, 2006, **18**, 2101–2104.
26 J. Perelaer, R. Jani, M. Grouchko, A. Kamyshny, S. Magdassi and U. S. Schubert, *Adv. Mater.*, 2012, **24**, 3993–3998.
27 G. Cummins and M. P. Y. Desmulliez, *Circuit World*, 2012, **38**, 193–213.
28 A. Rae and D. Hammer-Fritzinger, *Solid State Technol.*, 2006, **49**, 53–56.
29 M. Grouchko, A. Kamyshny, C. F. Mihailescu, D. F. Anghel and S. Magdassi, *ACS Nano*, 2011, **5**, 3354–3359.
30 F. M. Wolf, J. Perelaer, S. Stumpf, D. Bollen, F. Kriebel and U. S. Schubert, *J. Mater. Res.*, 2013, **28**, 1254–1261.
31 S. Choudhary, J. V. N. Sarma, S. Pande, S. Ababou-Girard, P. Turban, B. Lepine and S. Gangopadhyay, *AIP Adv.*, 2018, **8**, 055114.
32 S. Magdassi, M. Grouchko and A. Kamyshny, *Materials*, 2010, **3**, 4626–4638.
33 S. Jeong, K. Woo, D. Kim, S. Lim, J. S. Kim, H. Shin, Y. Xia and J. Moon, *Adv. Funct. Mater.*, 2008, **18**, 679–686.
34 Y. Kobayashi, S. Ishida, K. Ihara, Y. Yasuda, T. Morita and S. Yamada, *Colloid Polym. Sci.*, 2009, **287**, 877–880.
35 P. Pulkkinen, J. Shan, K. Leppänen, A. Känsäkoski, A. Laiho, M. Järn and H. Tenhu, *ACS Appl. Mater. Interfaces*, 2009, **1**, 519–525.
36 P. Kanninen, C. Johans, J. Merta and K. Kontturi, *J. Colloid Interface Sci.*, 2008, **318**, 88–95.
37 J. Li and C. Y. Liu, *New J. Chem.*, 2009, **33**, 1474–1477.
38 N. A. Luechinger, E. K. Athanassiou and W. J. Stark, *Nanotechnology*, 2008, **19**, 445201.
39 Y. Kobayashi and T. Sakuraba, *Colloids Surf., A*, 2008, **317**, 756–759.
40 T. G. Kim, H. J. Park, K. Woo, S. Jeong, Y. Choi and S. Y. Lee, *ACS Appl. Mater. Interfaces*, 2018, **10**, 1059–1066.
41 M. Grouchko, A. Kamyshny and S. Magdassi, *J. Mater. Chem.*, 2009, **19**, 3057.
42 Z. Chen, D. Mochizuki, M. M. Maitani and Y. Wada, *Nanotechnology*, 2013, **24**, 1–9.
43 J. I. Njagi, C. M. Netzband and D. V. Goia, *J. Colloid Interface Sci.*, 2017, **488**, 72–78.
44 C. Tsai, S. Chen, J. Song, I. Chen and H. Lee, *Corros. Sci.*, 2013, **74**, 123–129.
45 B. Zhang, W. Li, J. Jiu, Y. Yang, J. Jing, K. Suganuma and C. Li, *Inorg. Chem.*, 2019, **58**, 3374–3381.
46 S. S. Chee and J. H. Lee, *Mater. Chem. Phys.*, 2017, **185**, 176–182.
47 J. Li, X. Yu, T. Shi, C. Cheng, J. Fan, S. Cheng, T. Li, G. Liao and Z. Tang, *J. Alloys Compd.*, 2017, **709**, 700–707.
48 C. K. Kim, G. J. Lee, M. K. Lee and C. K. Rhee, *Powder Technol.*, 2014, **263**, 1–6.
49 R. Zhang, W. Lin, K. Lawrence and C. P. Wong, *Int. J. Adhes. Adhes.*, 2010, **30**, 403–407.
50 T. Michaud and S. S. Nobre, *J. Nanoparticle Res.*, 2019, **21**, 116.
51 G. Yang, P. Wang, Y. Liu, S. Lu, B. Luo, T. Lai, S. Ta, T. Lin, J. Luo, Y. Zhang and C. Cui, *J. Alloys Compd.*, 2022, **923**, 166271.


 

52 Y. Tian, Z. Jiang, C. Wang, S. Ding, J. Wen, Z. Liu and C. Wang, *RSC Adv.*, 2016, **6**, 91783–91790.
53 S. W. Park, T. Sugahara, M. Hatamura, N. Kagami, S. Sakamoto, S. Nagao and K. Suganuma, *Mater. Lett.*, 2015, **151**, 68–71.
54 S.-S. Chee and J.-H. Lee, *J. Mater. Chem. C*, 2014, **2**, 5372–5381.
55 W. Li, D. Hu, L. Li, C. Li, J. Jiu, C. Chen, T. Ishina, T. Sugahara and K. Suganuma, *ACS Appl. Mater. Interfaces*, 2017, 24711–24721.
56 A. Pajor-Świerzy, Y. Farraj, A. Kamyshny and S. Magdassi, *Colloids Surf., A*, 2017, **522**, 320–327.
57 A. Pajor-Świerzy, Y. Farraj, A. Kamyshny and S. Magdassi, *Colloids Surf., A*, 2017, **521**, 272–280.
58 C. Yim, A. Sandwell and S. S. Park, *ACS Appl. Mater. Interfaces*, 2016, **8**, 22369–22373.
59 Y. S. Park, C. Y. An, P. K. Kannan, N. Seo, K. Zhuo, T. K. Yoo and C. H. Chung, *Appl. Surf. Sci.*, 2016, **389**, 865–873.
60 S. J. Kim, E. A. Stach and C. A. Handwerker, *Appl. Phys. Lett.*, 2010, **96**, 1–3.
61 X. Yu, J. Li, T. Shi, C. Cheng, G. Liao, J. Fan, T. Li and Z. Tang, *J. Alloys Compd.*, 2017, **724**, 365–372.
62 Q. Jia, G. Zou, W. Wang, H. Ren, H. Zhang, Z. Deng and B. Feng, *ACS Appl. Mater. Interfaces*, 2020, **12**, 16743–16752.
63 W. Zhang, Y. Zhou, Y. Ding, L. Song and Q. Yuan, *Appl. Surf. Sci.*, 2022, **586**, 152691.
64 M. Deng and V. Subramanian, *ACS Appl. Electron. Mater.*, 2022, **4**, 4929–4935.
65 B. K. Park, D. Kim, S. Jeong, J. Moon and J. S. Kim, *Thin Solid Films*, 2007, **515**, 7706–7711.
66 A. Yabuki and N. Arriffin, *Thin Solid Films*, 2010, **518**, 7033–7037.
67 K. Woo, D. Kim, J. S. Kim, S. Lim and J. Moon, *Langmuir*, 2009, **25**, 429–433.
68 B. Abbas, E. Jewell and J. Searle, *J. Electron. Mater.*, 2024, **53**, 2498–2503.
69 H. S. Kim, S. R. Dhage, D. E. Shim and H. T. Hahn, *Appl. Phys. A: Mater. Sci. Process.*, 2009, **97**, 791–798.
70 H. Kim, J. Ryu, H. Kim and H. T. Hahn, *J. Electron. Mater.*, 2011, **40**, 42–50.
71 D. Dai and D. Gu, *J. Mater.*, 2014, **55**, 482–491.
72 E. Halonen, E. Heinonen and M. Mäntysalo, *Opt. Photonics J.*, 2013, **03**, 40–44.
73 J. Niittynen, E. Sowade, H. Kang, R. R. Baumann and M. Mäntysalo, *Sci. Rep.*, 2015, **5**, 1–10.
74 J. Kwon, H. Cho, H. Eom, H. Lee, Y. D. Suh, H. Moon, J. Shin, S. Hong and S. H. Ko, *ACS Appl. Mater. Interfaces*, 2016, **8**, 11575–11582.
75 M. Zenou, O. Ermak, A. Saar and Z. Kotler, *J. Phys. D: Appl. Phys.*, 2014, **47**, 1–11.
76 P. Martins, N. Pereira, A. C. Lima, A. Garcia, R. Policia and V. Correia, *Adv. Funct. Mater.*, 2023, **33**, 2213744.
77 W. Li, Q. Sun, L. Li, J. Jiu, X. Liu, M. Kanehara, T. Minari and K. Suganuma, *Appl. Mater. Today*, 2020, **18**, 100451.
78 E. Lester, G. Aksomaityte, J. Li, S. Gomez, J. Gonzalez-Gonzalez and M. Poliakoff, *Prog. Cryst. Growth Charact. Mater.*, 2012, **58**, 3–13.
79 G. Aksomaityte, M. Poliakoff and E. Lester, *Chem. Eng. Sci.*, 2013, **85**, 2–10.
80 P. W. Dunne, A. S. Munn, C. L. Starkey, T. A. Huddle and E. H. Lester, *Philos. Trans. R. Soc., A*, 2015, **373**, 1–21.
81 P. W. Dunne, E. Lester, C. Starkey, I. Clark, Y. Chen and A. S. Munn. in *Green Chemistry Series No. 57 Supercritical and Other High-pressure Solvent Systems: For Extraction, Reaction and Material Processing*, The Royal Society of Chemistry, 2018. pp. 449–475.
82 E. Lester, P. Blood, J. Denyer, D. Giddings, B. Azzopardi and M. Poliakoff, *J. Supercrit. Fluids*, 2006, **37**, 209–214.
83 British Standards Institute. at (2009) 1–52.
84 L. H. Schwartz and J. B. Cohen, *Diffraction from materials*, Springer-Verlag, Berlin Heidelberg GmbH, 1987.
85 H. T. Hai, H. Takamura and J. Koike, *J. Alloys Compd.*, 2013, **564**, 71–77.
86 C. Lee, N. R. Kim, J. Koo, Y. J. Lee and H. M. Lee, *Nanotechnology*, 2015, **26**, 455601.
87 M. Ross, *Phys. Rev.*, 1969, **184**, 233–242.
88 G. Bernard and C. H. P. Lupis, *Metall. Trans.*, 1971, **2**, 555–559.
89 D. A. Harrison, D. Yan and S. Blairs, *J. Chem. Thermodyn.*, 1977, **9**, 1111–1119.
90 Z. S. Pereira and E. Z. Da Silva, *J. Phys. Chem. C*, 2011, **115**, 22870–22876.
91 S. Bhagat, N. D. Theodore, S. Chenna and T. Alford, *Appl. Phys. Express*, 2009, **2**, 1–4.
92 W. Zhang, Y. Zhou, Y. Ding, L. Song, Q. Yuan, W. Zhao, C. Xu, J. Wei, M. Li and H. Ji, *Appl. Surf. Sci.*, 2022, **586**, 152691.
93 G. Yang, P. Wang, Y. Liu, S. Lu, B. Luo, T. Lai, S. Ta, T. Lin, J. Luo, Y. Zhang and C. Cui, *J. Alloys Compd.*, 2022, **923**, 166271.
94 X. Wang, Z. Yang, G. Zhang, J. Zhang and P. Liu, *Proc. - Electron. Compon. Technol. Conf.*, 2023, 1982–19882023-May.
95 Z. Wen, W. Liu, C. Hang, R. An and Y. Tian, *J. Mater. Res. Technol.*, 2024, **33**, 9123–9134.
96 Money Metals Exchange. (2019).
97 A. Bobsin, T. C. Rodrigues, I. J. Fernandes, S. B. Ferreira, C. R. Peter, W. Hasenkamp and C. A. M. Moraes, *Mater. Chem. Phys.*, 2024, **315**, 1–9.
98 M. Yu, J. Feng, S. P. Xie, Y. Wang, Y. Li, R. Wang, G. Lu, K. Li, R. Wu, W. Zhao and Y. Tian, *J. Alloys Compd.*, 2025, **1024**, 179870.
99 Y. C. Huang, P. H. Tseng, K. S. Ho and Y. M. Wang, *Mater. Chem. Phys.*, 2025, **339**, 130641.
100 S. Sudhakar, K. N. Arya, A. S. Pillai, S. A. Jose, A. Chandran and S. K. Peethambharan, *J. Mater. Chem. C*, 2025, 21481–21497.
101 Y. Zhou, P. Vasko, Y. Zhu, J. Wang, C. Kalha, A. Regoutz, A. Hashibon, Y. Tai, G. B. Hwang and C. E. Knapp, *Small Methods*, 2025, **9**, 1–12.